Supplementary Information (SI) for

Enhanced Carrier Extraction and Photostability in Perovskite Solar Cells via Band-Engineered Sb_2O_x/TiO_2 Bilayer Heterojunction

Nasrin Siraj Lopa,[a, ‡] Yuna Choi,[a, ‡] Md. Mahbubur Rahman,[a] and Tae Woong Kim [a,b,*]

[a]Department of Energy Materials Science & Engineering, College of Science and Technology, Konkuk University, Chungcheongbuk-do 27478, Republic of Korea

[b]Center for Science and Technology Convergence Research, Konkuk University, Chungcheongbuk-do 27478, Republic of Korea

‡N. S. Lopa and Y. Choi contributed equally to this work

*E-mail: taewoongkim@kku.ac.kr

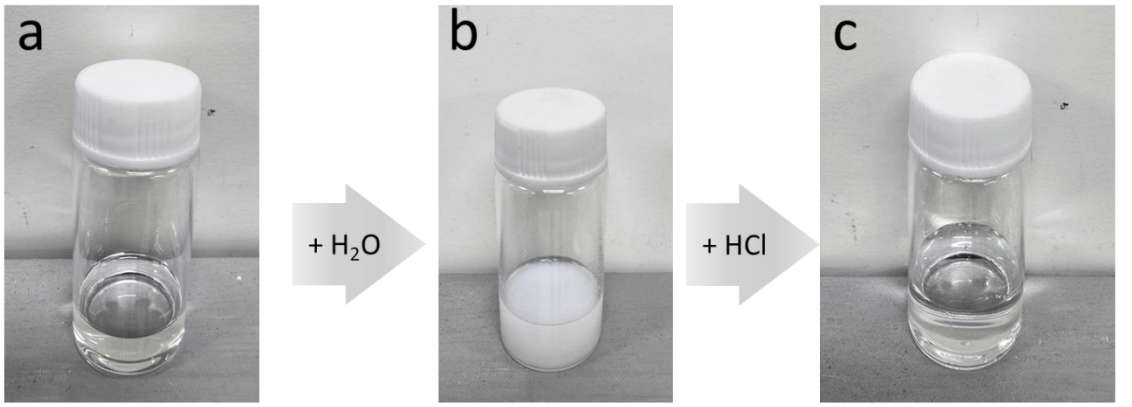

Fig. S1. Photographs illustrating the stepwise preparation of the antimony oxide precursor solution: (a) dissolution of $SbCl_3$ powder in ethanol to form a clear solution, (b) formation of antimony oxide micelles upon gradual addition of deionized water, and (c) generation of a transparent and homogeneous hydrolysate after the introduction of concentrated HCl.

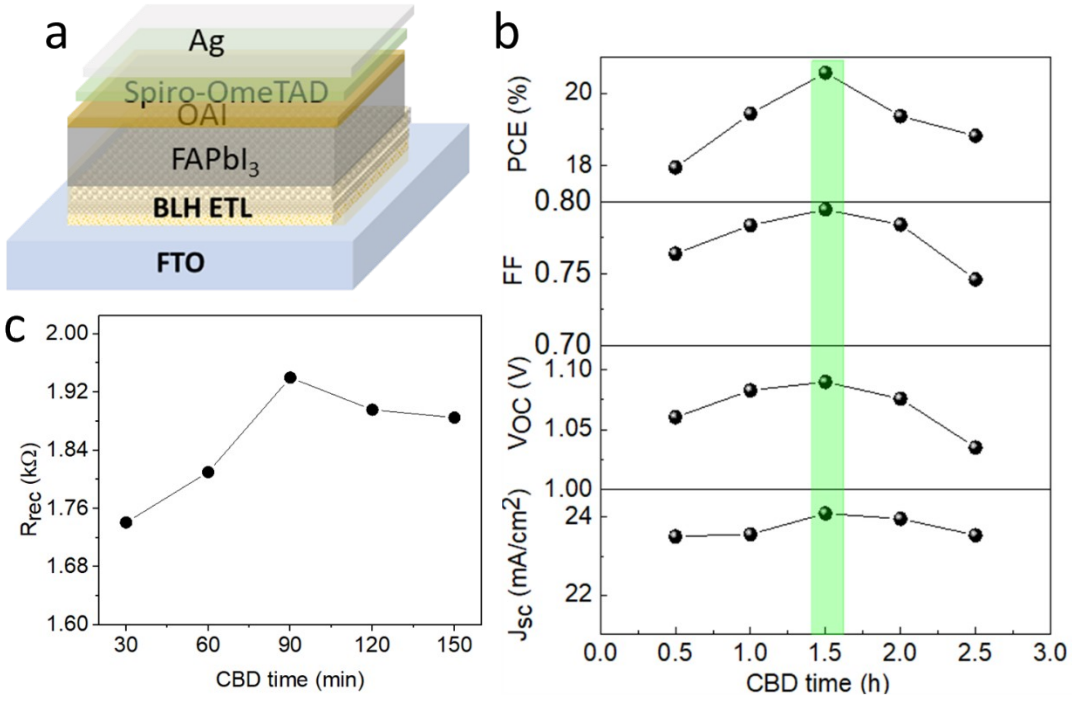

Fig. S2. (a) Schematic illustration of the planar PSC architecture. (b, c) Photovoltaic parameters (J_{sc}, V_{oc}, FF, and PCE) and R_{rec} of BLH-based PSCs as a function of Sb_2O_x deposition time. The R_{rec} values were extracted from Nyquist plots measured under dark conditions at an applied bias of 0.8 V.

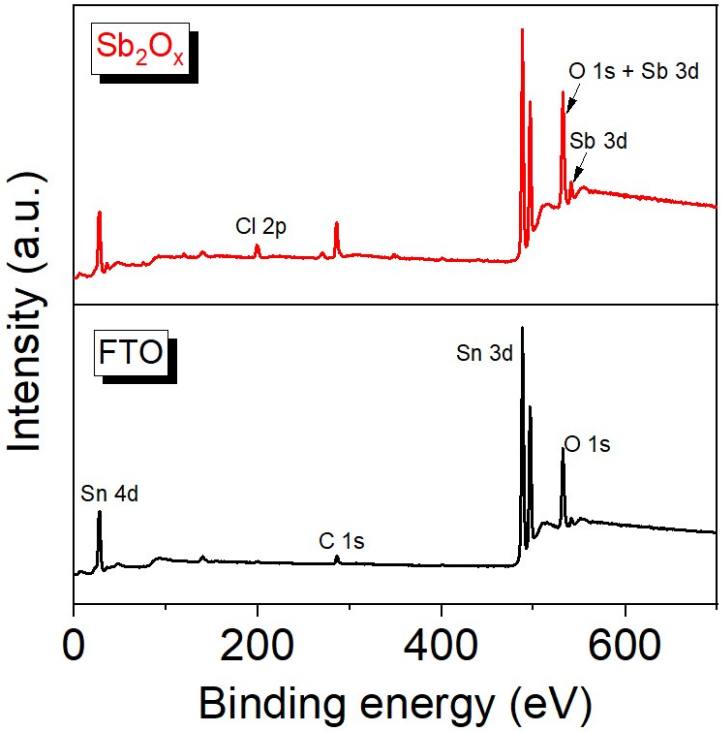

Fig. S3. Survey XPS spectra of bare FTO and Sb_2O_x-coated FTO substrate.

Table S1. Peak fitting parameters obtained from the XPS spectra of bare FTO and Sb_2O_x-coated FTO substrate.

		O 1s	**Sb**	
FTO		O-Sn	-	-
	Binding energy (ev)	531.10		
	Peak area	306830.31		
Sb_2O_x-coated FTO		O-Sn + Sb $3d_{5/2}$ + O-Sb	Sb $3d_{3/2}$	Sb $3d_{5/2}$
	Binding energy (ev)	530.98	540.35	-
	Peak area	519527	101461.83	152192.74

Stoichiometric calculation of Sb_2O_x

The total O 1s peak area for the Sb_2O_x-coated FTO substrate was 519527, while the corresponding O–Sn signal from the bare FTO was 306830.31. Subtracting the latter yielded an excess O 1s area of 212696.70, which accounts for both the oxygen bonded to antimony (O–Sb) and the overlapping Sb $3d_{5/2}$ contribution.[S1] Using the known ratio that the area of Sb $3d_{5/2}$ is 1.5 times that of Sb $3d_{3/2}$,[S2] and given the Sb $3d_{3/2}$ area as 101461.83, the estimated area for Sb $3d_{5/2}$ was calculated to be 152192.74. Subtracting this from the excess O 1s signal gave a net O–Sb contribution of 60503.95. After normalizing using the relative sensitivity factors (RSF = 2.93 for O 1s and 16.39 for Sb $3d_{5/2}$),[S3] the corrected signal intensities were 20649.80 for O–Sb and 9285.70 for Sb. This results in an atomic ratio of O to Sb of approximately 2.22.

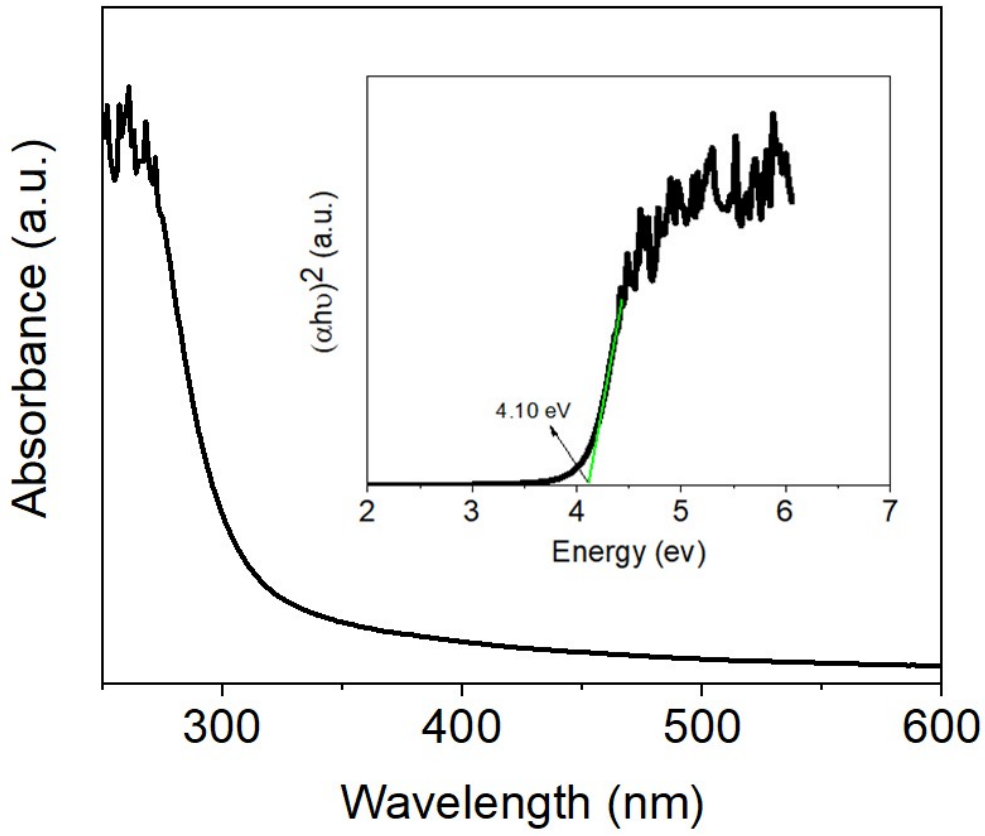

Fig. S4. UV–vis absorption spectrum of the Sb_2O_x layer deposited on a silica glass substrate. The inset displays the corresponding Tauc plot used to estimate the optical bandgap.

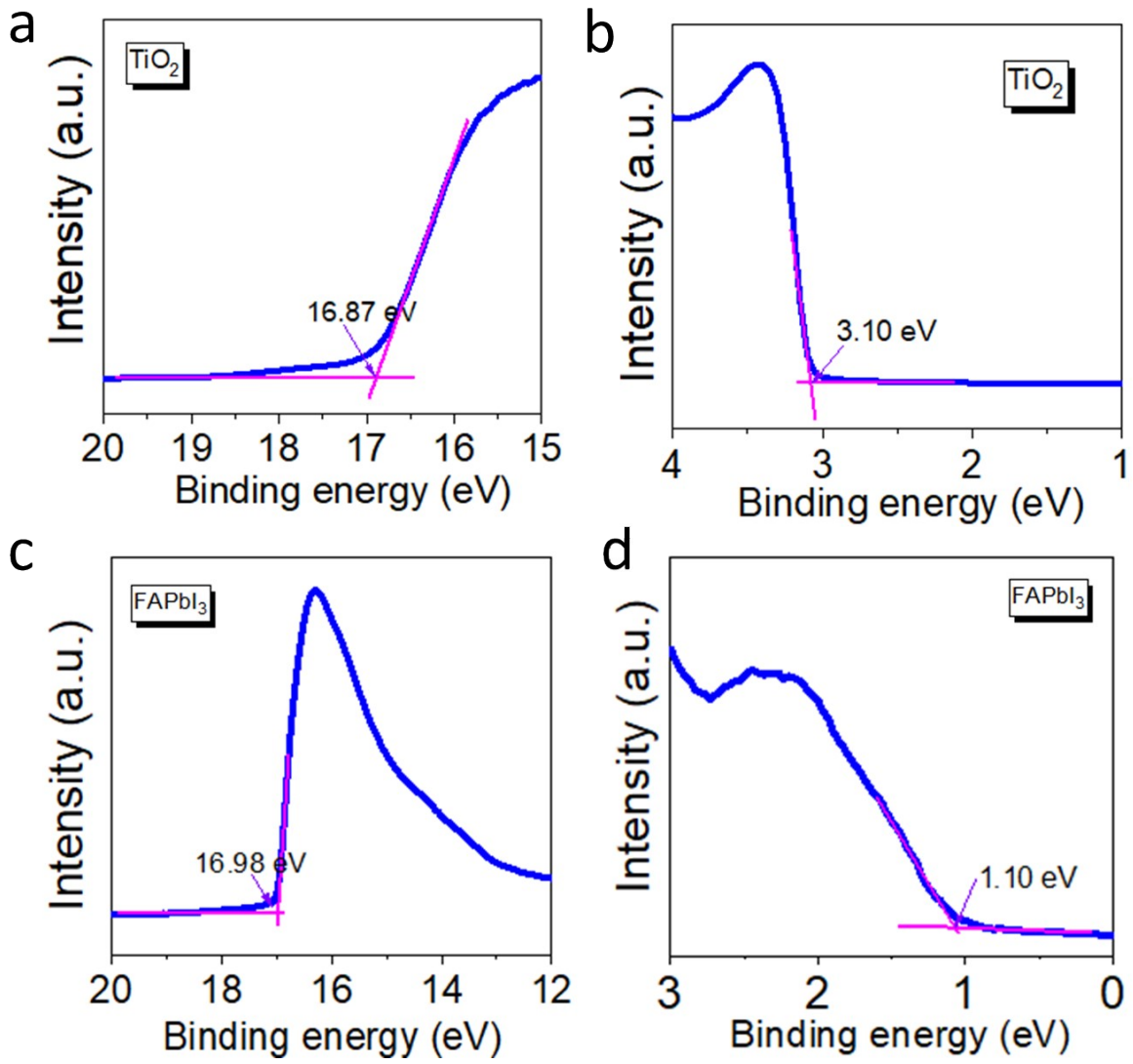

Fig. S5. Ultraviolet photoelectron spectroscopy (UPS) spectra of (a, b) the TiO_2 layer and (c, d) the $FAPbI_3$ layer, showing the secondary electron cutoff and valence band region, respectively.

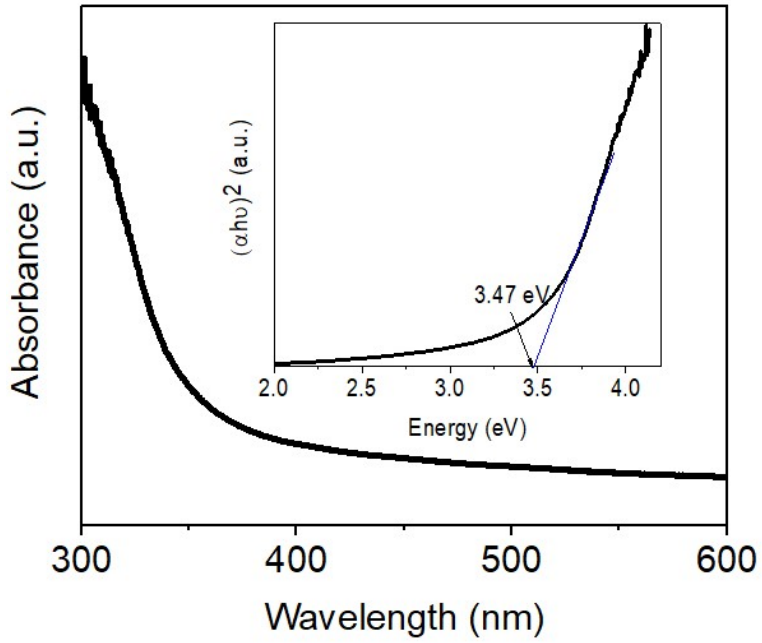

Fig. S6. UV-vis absorption spectrum of the TiO_2 layer. The inset displays the corresponding Tauc plot.

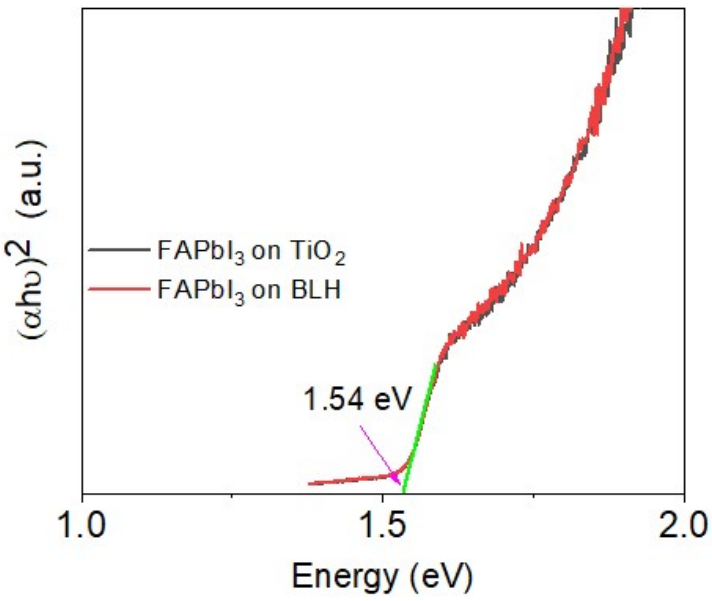

Fig. S7. Tauc plot derived from the UV-vis absorption spectrum of the $FAPbI_3$ layer, used to estimate its optical bandgap.

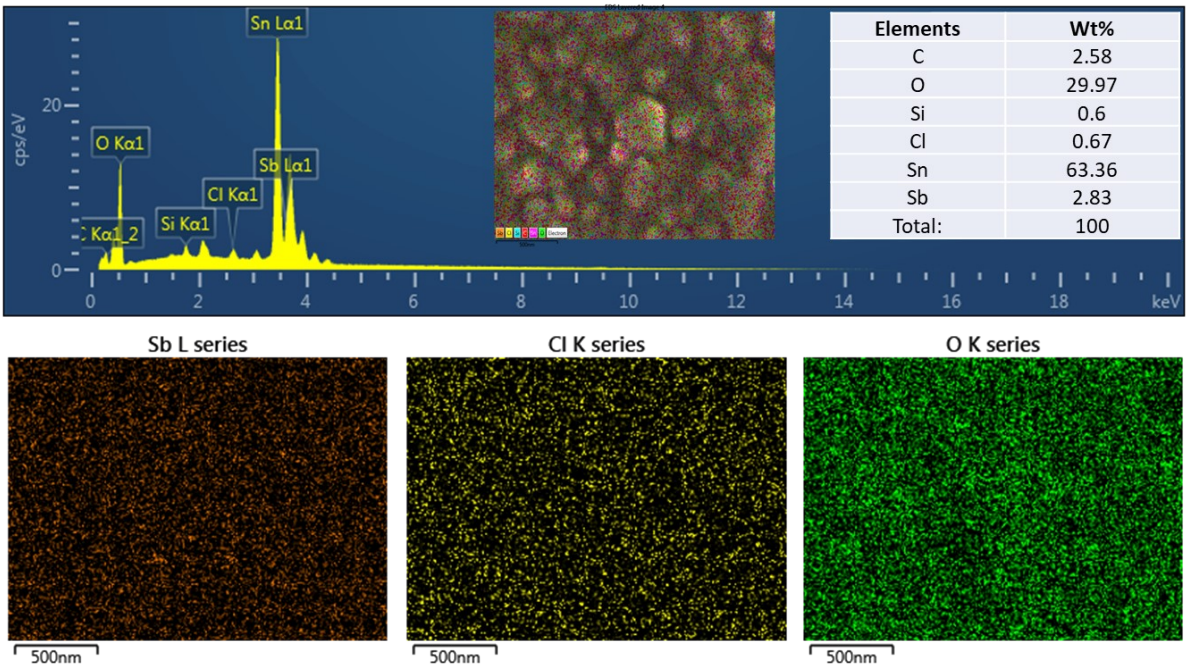

Fig. S8. EDX spectrum and elemental mapping of Sb, O, and Cl for the Sb_2O_x-coated FTO substrate. The inset displays the corresponding FE-SEM image along with the elemental weight percentages.

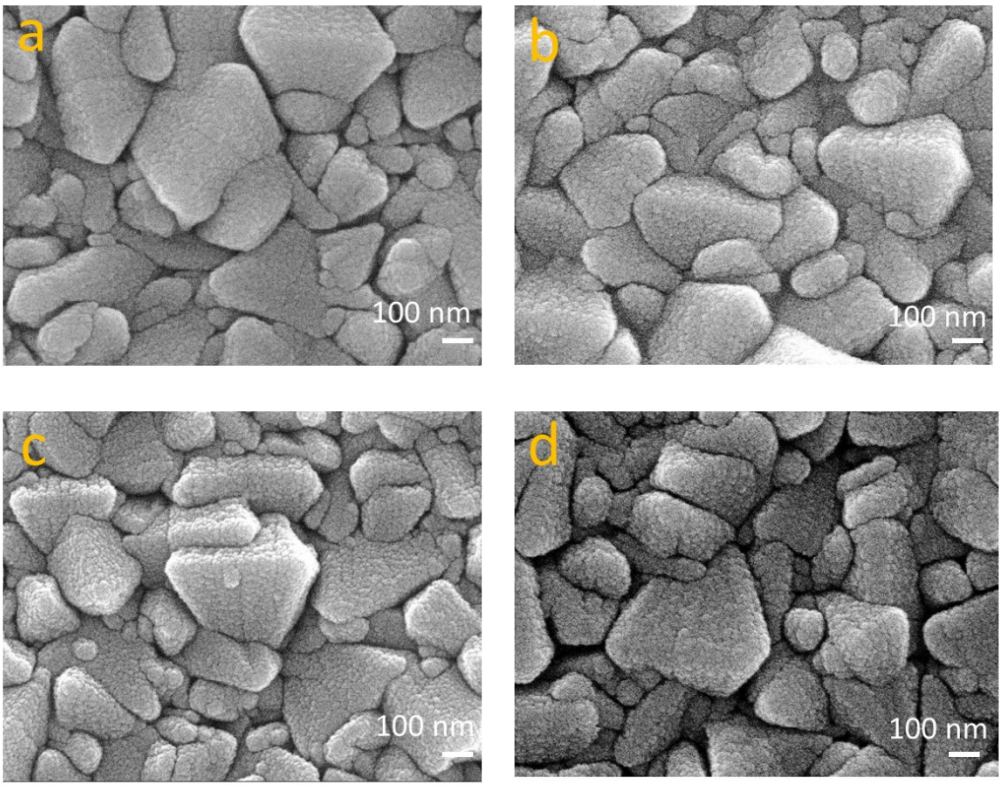

Fig. S9. Top-view FE-SEM images of Sb_2O_x layers deposited on FTO substrates with varying deposition times of 0.5, 1, 2, and 2.5 h.

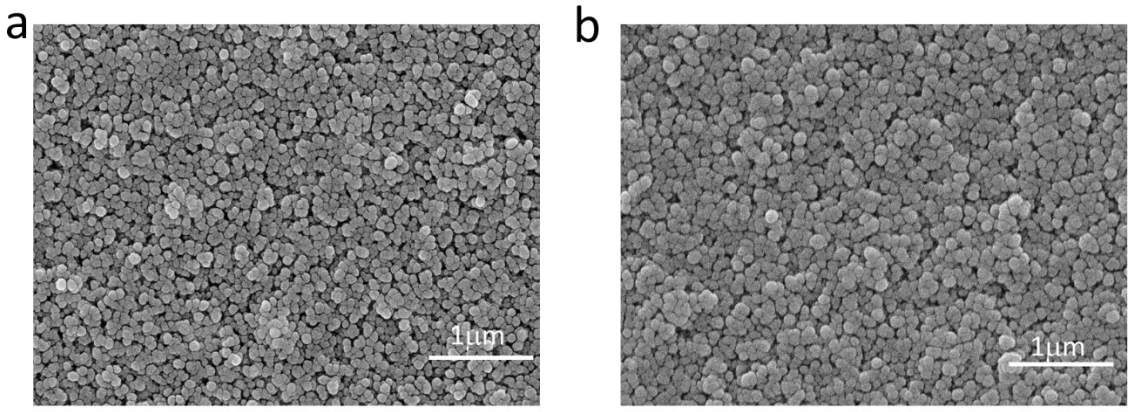

Fig. S10. Top-view FE-SEM images of mesoporous TiO_2 (m-TiO_2) layers deposited on compact TiO_2 (c-TiO_2) and Sb_2O_x substrates.

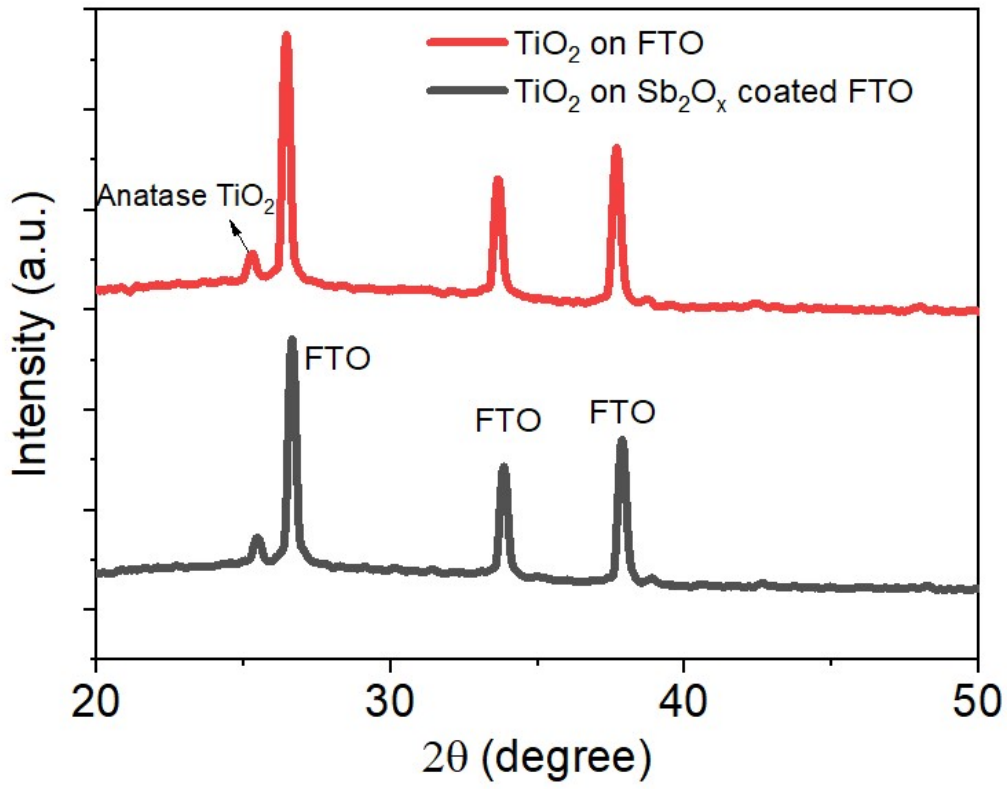

Fig. S11. XRD patterns of TiO_2 layers deposited on bare FTO and Sb_2O_x-coated FTO substrates.

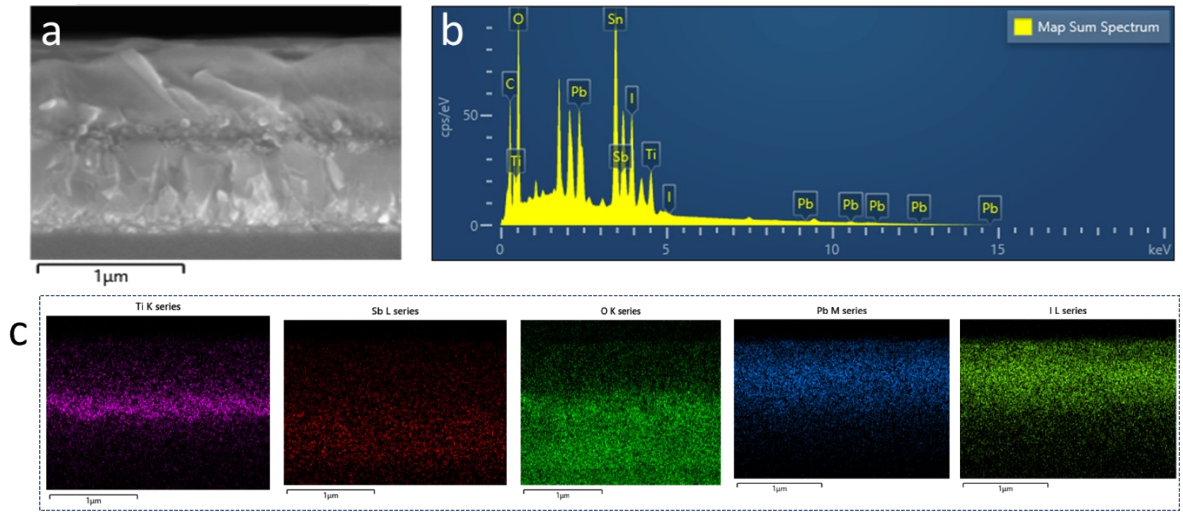

Fig. S12. (a) Cross-sectional FE-SEM image of the Sb_2O_x/TiO_2/perovskite interface. (b) Corresponding EDS spectra. (c) Elemental mapping showing the spatial distribution of Ti, Sb, O, Pb, and I.

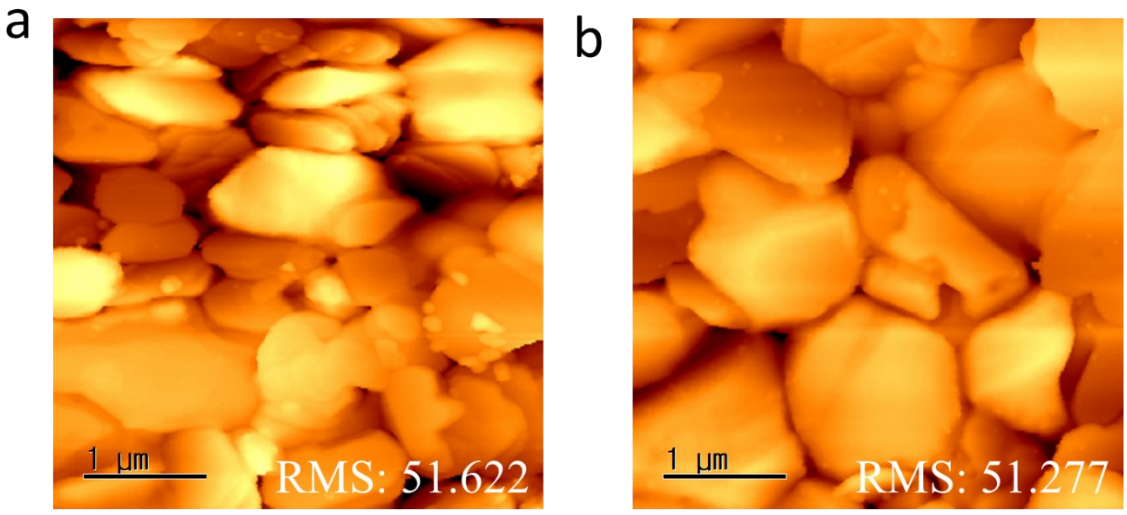

Fig. S13. AFM images of $FAPbI_3$ layers formed on (a) TiO_2- and (b) BLH-coated FTO substrate.

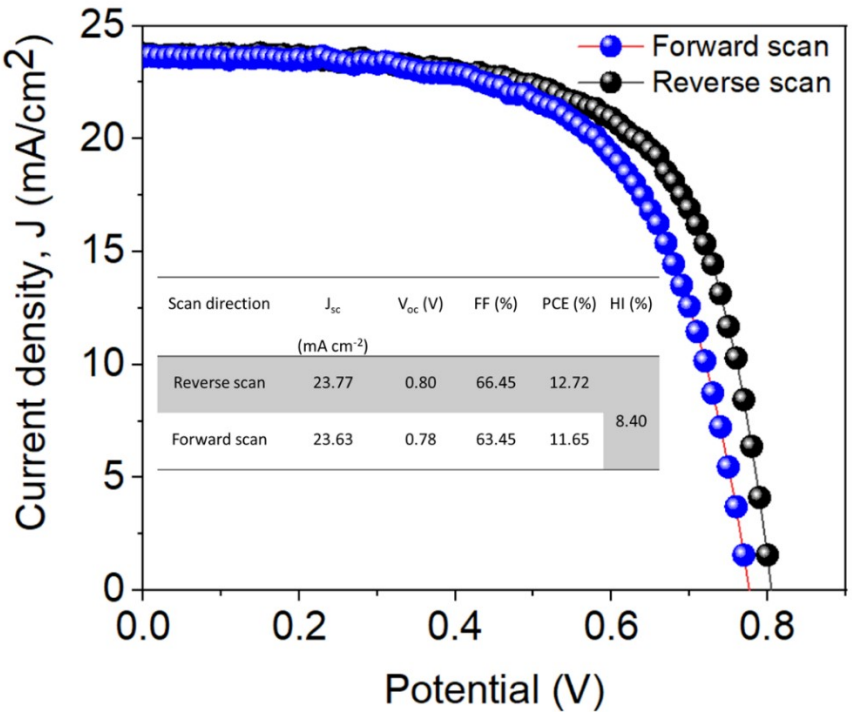

Fig. S14. J-V characteristics of the Sb_2O_x-based PSC measured under both reverse and forward

scan directions. The inset displays the corresponding photovoltaic parameters for each scan.

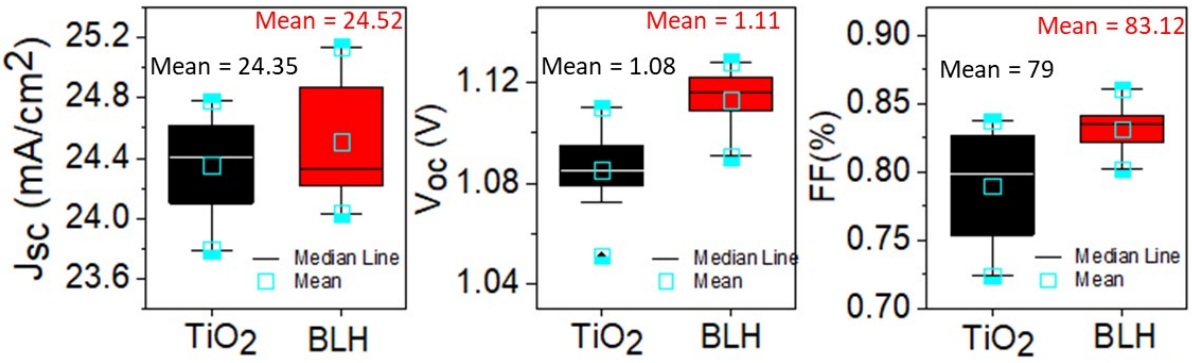

Fig. S15. Statistical distribution of the PV parameters (V_{oc}, J_{SC}, FF) of TiO_2- and BLH-ETLs-based PSCs.

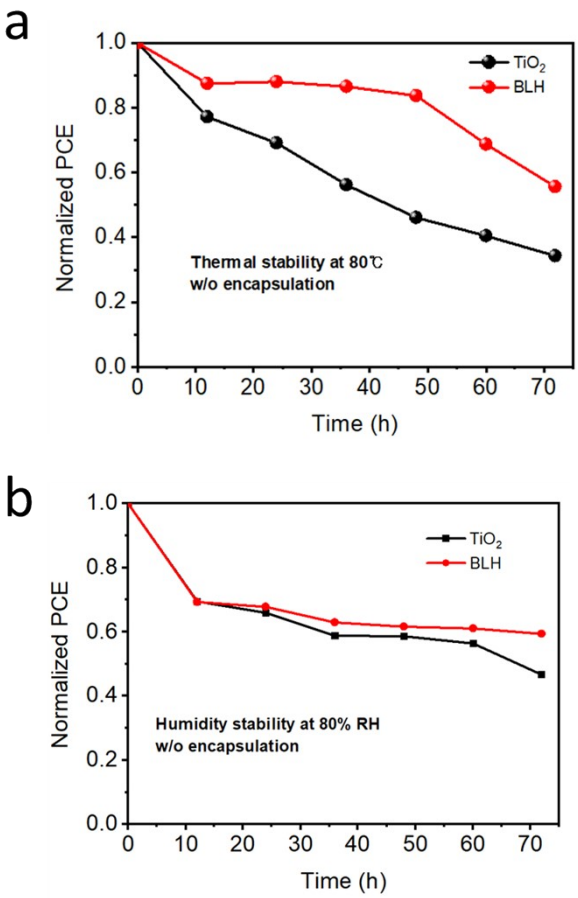

Fig. S16. Stability evaluation of PSCs: (a) thermal stability at 80 °C in ambient air and (b)

humidity stability at 80% RH in ambient air without encapsulation.

Table S2. Comparison of the photovoltaic performance of various reported bilayer ETL-based PSCs with Sb_2O_x/TiO_2 ETL-based PSCs, including details on PCE, perovskite materials, and device structures.

ETLs	Perovskite	Device structure	PCE (%)	Ref.
c-$TiO_2/Fe_2O_3/SnO_2$	$CsPbBr_3$	n-i-p	10.23	S4
Bilayer SnO_2	$MAPbI_3$		17.61	S5
TiO_2/SnO_2	Cs/FA/MA perovskite		17.64	S6
TiO_2/SnO_2	MA/FA perovskite		23.45	S7
TiO_2/SnO_2	Cs/MA/FA perovskite		15.39	S8
TiO_2/SnO_2-quantum dots	MA/FA perovskite		10.41	S9
TiO_2/TiO_2	$MAPbI_3$		14.143	S10
ZnO/SnO_2	$MAPbI_3$		20.43	S11
ZnO/TiO_x	MA/FA perovskite		19.34	S12
Sb_2O_x/TiO_2	$FAPbI_3$		23.72%	**This work**

Table S3. Photovoltaic parameters of PSCs incorporating SnO_2/TiO_2 BLH ETLs.

Cell number	J_{sc} (mA/cm^2)	V_{oc} (V)	FF	PCE (%)
1	22.70	1.04	0.75	17.81
2	23.62	1.10	0.80	20.70
3	23.21	1.06	0.77	19.05
4	23.83	1.06	0.78	19.76
5	24.31	1.08	0.76	19.84
6	23.47	1.02	0.74	17.72
7	23.04	1.02	0.74	17.30
8	24.02	1.06	0.80	20.31
9	24.13	1.06	0.78	20.09
10	23.40	1.04	0.78	19.03
11	23.82	1.07	0.81	20.77
12	23.96	1.09	0.80	20.87
13	23.27	1.05	0.77	18.67
14	23.10	1.02	0.72	16.83
15	24.09	1.08	0.80	20.79
16	24.18	1.05	0.76	19.17
17	23.40	1.00	0.72	16.91
18	22.94	0.98	0.72	16.13
19	23.95	1.08	0.82	21.04
20	23.52	1.02	0.74	17.69
Average	**23.60±0.45**	**1.05±0.03**	**0.77±0.03**	**19.02 ±1.51**

Table S4. TRPL parameters obtained by fitting.

Sample	τ_1 (ns)	A_1	τ_2 (ns)	A_2	τ_{avg} (ns)
Sb_2O_x	230.15	0.18	1384.40	0.41	1305.88
TiO_2	114.52	0.19	607.64	0.28	551.70
BLH	86.35	0.08	425.0	0.21	400.0

The decay in PL intensity from the TRPL measurements was analyzed using a bi-exponential decay model [S13]:

$I = I_o + A_1 \exp\left(\frac{x}{\tau_1}\right) + A_2 \exp\left(\frac{x}{\tau_2}\right)$, where τ_1 represents the fast decay component associated with interfacial charge transfer at the ETL/perovskite interface and τ_2 denotes the slower component, attributed to radiative recombination of free carriers within the bulk $FAPbI_3$ layer. The average lifetime (τ_{avg}) was calculated using the equation $\tau_{avg} = (A_1\tau_1^2 + A_2\tau_2^2)/(A_1\tau_1 + A_2\tau_2)$. [S13]

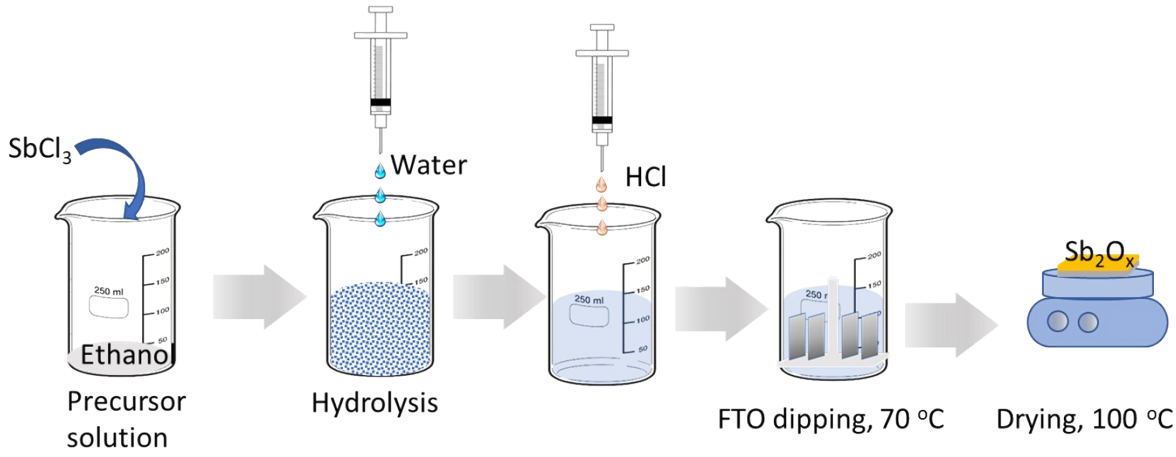

Fig. S17. Stepwise schematic diagram of the chemical bath deposition (CBD) process for forming antimony oxide (Sb_2O_x) layers on FTO substrates.

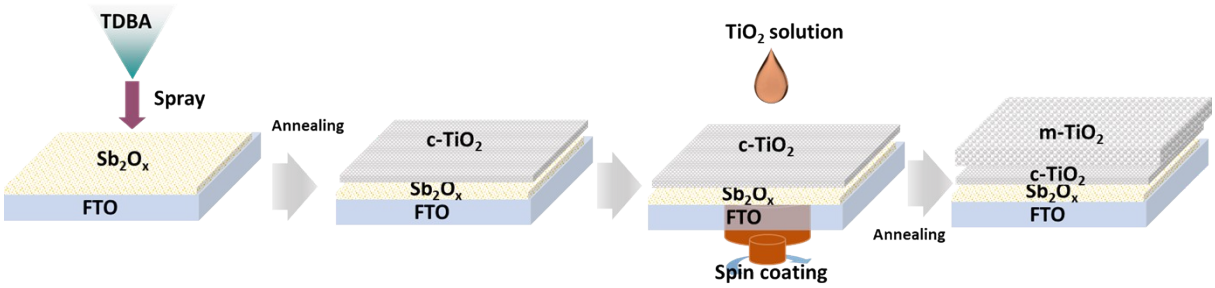

Fig. S18. Schematic illustration of the deposition of compact and mesoporous TiO_2 layers onto Sb_2O_x layers.

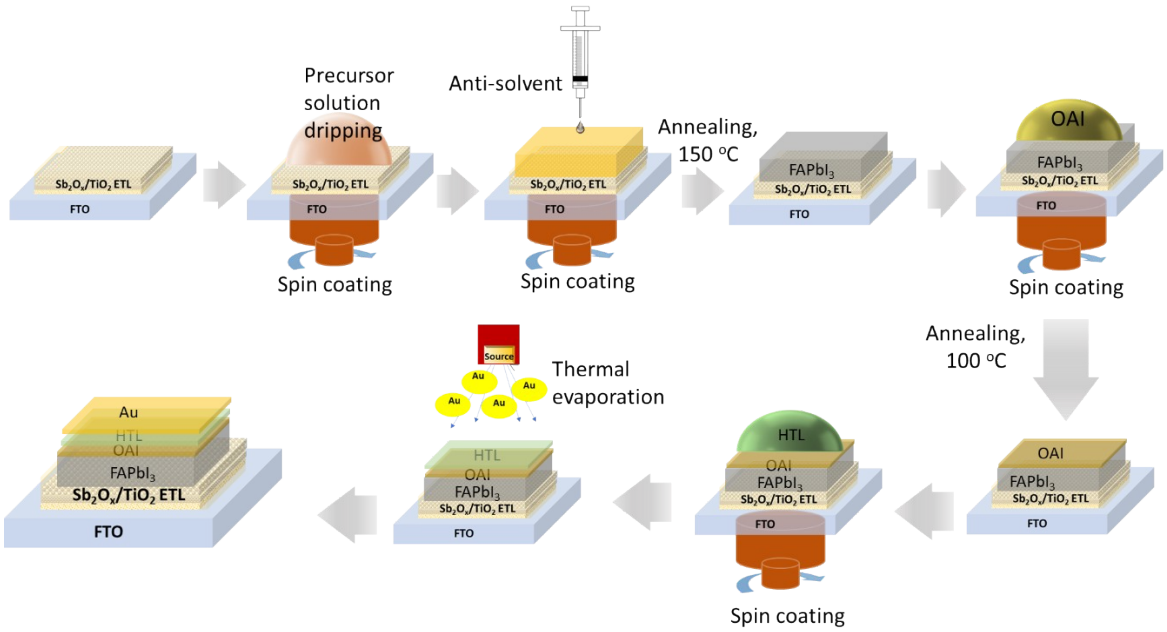

Fig. S19. Schematic diagram of the fabrication of perovskite solar cells using Sb_2O_x/TiO_2 heterostructure electron transport layers (ETLs).

References

S1. X. Ling, J. Guo, Y. Li, C. Shen, Y. Wang, X. Zhang, X. Zhao, H. Wang, X. Yuan, J. Shi, Y. Li, S. Chen, J. Yuan and Y. Deng, Chemical Bath Deposited Antimony Oxide Thin Films for Efficient Perovskite Solar Cells, *Nano Lett.,* 2021, **24**, 9065−9073.

S2. O. E. Linarez Perez, M. D. Sanchez and M. L. Teijelo, Characterization of growth of anodic antimony oxide films by ellipsometry and XPS, *J. Electroanal. Chem.,* 2010*,* **645**, 143−148.

S3. Case Study: Quantification of O/In/Sb/C using an Effective RSF and Tags, Casa Software Ltd. www.casaxps.com.

S4. R. Tui, H. Sui, J. Mao, X. Sun, H. Chen, Y. Duan, P. Yang, Q. Tang and B. He, Round-comb Fe_2O_3@SnO_2 heterostructures enable efficient light harvesting and charge extraction for high-performance all-inorganic perovskite solar cells, *J. Colloid Interface Sci.*, 2023, **640**, 918–927.

S5. H. Yi, D. Wang, M. A. Mahmud, F. Haque, M. B. Upama, X. Xu, L. Duan and A. Uddin, Bilayer SnO_2 as Electron Transport Layer for Highly Efficient Perovskite Solar Cells, *ACS Appl. Energy Mater.*, 2018, **1**, 6027–6039.

S6. X. Sun, L. Li, S. Shen and F. Wang, TiO_2/SnO_2 Bilayer Electron Transport Layer for High Efficiency Perovskite Solar Cells, *Nanomaterials*, 2023, **13**, 249.

S7. Y. Ko, T. Kim, C. Lee, C. Lee, Y. J. Yun and Y. Jun, Alleviating Interfacial Recombination of Heterojunction Electron Transport Layer via Oxygen Vacancy Engineering for Efficient Perovskite Solar Cells Over 23%, *Energy Environ. Mater.*, 2023, **6**, e12347.

S8. Z. Liu, B. Sun, X. Liu, J. Han, H. Ye, Y. Tu, C. Chen, T. Shi, Z. Tang and G. Liao, 15% efficient carbon based planar-heterojunction perovskite solar cells using TiO_2/SnO_2 bilayer as electron transport layer, J. Mater. Chem. A, 2018, **6**, 7409-7419.

S9.A.G. Mirea, I.D. Vlaicu, S. Derbali, F. Neatu, A.G. Tomulescu, C. Besleaga, M. Enculesc

u, A.C. Kuncser, A.C. Iacoban, N. Filipoiu, M. Cuzminschi, G.A. Nemnes, A. Manolesc, M. Florea and I. Pintilie, Electron transporting bilayers for perovskite solar cells: Spray coating deposition of c-TiO_2/m SnO_2-quantum dots, *Coll. Surf. A Physicochem. Eng. Asp.*, 2025, **705**, 135508.

S10. M. H. Nguyen, S.-H. Yoon and K.-S. Kim, Hydrothermally fabricated TiO_2 heterostructure boosts efficiency of $MAPbI_3$ perovskite solar cells, *J. Ind. Eng. Chem.*, 2022, **106**, 382–392.

S11. Y. W. Noh, I. S. Jin, K. S. Kim, S. H. Park and J. W. Jung, Reduced Energy Loss in SnO_2/ZnO Bilayer Electron Transport Layer-Based Perovskite Solar Cells for Achieving High Efficiencies in Outdoor/Indoor Environments, *J. Mater. Chem. A*, 2020, **8**, 17163-17173.

S12. J. Ma, Z. Lin, X. Guo, J. He, Z. Hu, J. Su, J. Zhang, J. Chang and Y. Hao, Low temperature ZnO/TiO_x electron-transport layer processed from aqueous solution for highly efficient and stable planar perovskite solar cells, *Mater. Today Energy*, 2019, **14**, 100351.

S13. M. M. Rahman, S. H. Won, H. D. Son, H. J. Jeong and T. W. Kim, Boosting the efficiency of perovskite solar cells through molecular interface-driven grain and defect control, *Mater. Today Energy*, 2025, **52**, 101939.